NMR 1D-imaging of water infiltration into mesoporous matrices

Steven Le Feunteun, Olivier Diat, Armel Guillermo, Arnaud Poulesquen, Renaud Podor

This file presents the 'accepted version' of the following original research article:

Le Feunteun, S., Diat, O., Guillermo, A., Poulesquen, A., & Podor, R. (2011). NMR 1D-imaging of water infiltration into mesoporous matrices. Magnetic Resonance Imaging, 29(3), 443–455. https://doi.org/10.1016/j.mri.2010.10.001

NMR 1D-imaging of water infiltration into mesoporous matrices

S. Le Feunteun[1,2], O. Diat[1], A. Guillermo[2], A. Poulesquen[3] and R. Podor[1]*

[1] ICSM – UMR 5257 (CEA, CNRS, UM2, ENCM), 30207 Bagnols sur Cèze, France

[2] CEA, INAC, SPrAM – UMR 5819 (CEA, CNRS, UJF), 38054 Grenoble Cedex 9, France

[3] CEA, DEN/MAR/DTCD/SPDE, 30207 Bagnols sur Cèze, France

* Corresponding author: Steven Le Feunteun; Tel.: +33 1 30 81 45 96; E-mail address: steven.le-feunteun@grignon.inra.fr

1

Abstract

It is shown that coupling NMR 1D-imaging with the measure of NMR relaxation times and self-diffusion coefficients can be a very powerful approach to investigate fluid infiltration into porous media. Such an experimental design was used to study the very slow seeping of pure water into hydrophobic materials. We consider here three model samples of nuclear waste conditioning matrices which consist in a dispersion of $NaNO_3$ (highly soluble) and/or $BaSO_4$ (poorly soluble) salt grains embedded in a bitumen matrix. Beyond studying the moisture progression according to the sample depth, we analyse the water NMR relaxation times and self-diffusion coefficients along its 1D concentration profile to obtain spatially resolved information on the solution properties and on the porous structure at different scales. It is also shown that, when the relaxation or self-diffusion properties are multimodal, the 1D-profile of each water population is recovered. Three main levels of information were disclosed along the depth-profiles. They concern i) the water uptake kinetics, ii) the salinity and the molecular dynamics of the infiltrated solutions and iii) the microstructure of the water-filled porosities: open networks coexisting with closed pores. All these findings were fully validated and enriched by NMR cryoporometry experiments and by performing Environmental Scanning Electronic Microscopy (ESEM) observations. Surprisingly, results clearly show that insoluble salts enhance the water progression and thereby increase the capability of the material to uptake water.

Keywords: porous media, relaxation times, PFG-NMR, restricted diffusion, pore size, bituminized waste product (BWP), leaching.

1. Introduction

The manifold measurements provided by Nuclear Magnetic Resonance (NMR) are widely used to investigate fluid transport within porous media. This is indeed an area of continuing research in various disciplines, such as civil engineering, soil and food sciences. Studies on drying or infiltrating processes generally resort to imaging techniques in order to characterise the spatial evolution of the fluid concentration over time. To do so, a common method consists in studying the fluid transport and/or the associated matrix swelling or shrinking in the axial symmetry of cylindrical samples by NMR 1D-imaging. Examples in the literature include, for instance, works on polymer membranes [1], organic hydrogels [2, 3], catalytic materials [4, 5] or porous building media [6]. Other studies resort to relaxation and self-diffusion experiments in order to understand how the fluid locally progresses and how the micro- and nanostructure of the material evolve. For instance, such approaches have been recently applied to investigate the modifications of the internal structure of gypsum [7, 8], cement pastes [9], and pharmaceutical pellets [10] caused by water absorption. Nevertheless, in contrast to imaging experiments, relaxation and self-diffusion measurements are averaged on the sample volume. Therefore, results generally consist in distributions of values that cannot be directly related to the macroscopic variations of the sample structure and composition induced by the fluid progression.

Studies that resort to NMR experiments with 1D spatial encoding are not so common even though they provide data that are spatially resolved along the sample depth-profile, thereby making possible to relate the information provided by the relaxation and self-diffusion measurements to the local sample composition. Such methods have nevertheless proven their efficiency for characterising the spatial dependence of micrometric droplet sizes in emulsified samples [11-13]. In this paper, we attempt to illustrate that combining NMR 1D-imaging with relaxation and self-diffusion studies can be a powerful method to investigate infiltrating or drying processes. To do so, we resort to an interesting approach that couples a specific NMR sequence, as spin-system

preparation, with 1D-imaging, as signal acquisition mode [11], and use it to investigate the moisture progression in some hydrophobic materials that are submitted to a unidirectional water infiltration. Beyond the water concentration 1D-profile at the macroscopic scale, the spatial dependence of the nano- and microporous structures are thus investigated along the depth-profiles by means of the relaxation or self-diffusion measurements, respectively.

The materials studied are called bituminized waste products (BWP) and consist in a dispersion of different salt grains, which contain a very small fraction of radioactive elements, embedded in a bitumen matrix [14]. Indeed, in France, a part of the low and intermediate radioactive elements coming from the effluents of the nuclear industry has been managed by their incorporation in bitumen. It is now established that the interaction of BWP with water in storage zones can lead to some material modifications, and hence deteriorate the conditioning over a very long period of time. Previous studies on the leaching of BWP have allowed scientists to put forward constitutive models aiming at predicting the kinetics of water uptake and salt release as well as the matrix microstructure deformation in the leached layer [14-16]. In this context, our study was motivated by the need of better characterising the behaviour of BWP when brought in contact with water before refining the current models. More precisely, our goal was threefold: i) to determine whether the wetting front is limited by the dissolution front of the soluble salts ($NaNO_3$), ii) to check for a possible influence of the insoluble salts ($BaSO_4$) on the water uptake kinetics, and iii) to study the water dynamics as well as the sample structure over a wide range of length-scales in the leached zone.

Three inactive and model BWP samples varying by their composition in embedded salts are studied. After a chemical and structural characterisation of the unleached materials (section 4.1), a first set of NMR and 1D-imaging experiments is used to investigate the kinetics of water uptake and the moisture progression as a function of sample depth (sections 4.2 and 4.3). 1D-imaging measurements of relaxation times and self-diffusion coefficients are then exploited to locally

characterise the altered matrices along their depth (sections 4.4 and 4.6). Results provide information on the salinity of the infiltrated solution and on the structure of the porosity at different scales: an open network coexisting with closed pores at the micrometre scale, hindrance of the molecular dynamics in the wetting front, etc. All our findings are discussed in relation to the composition of the different samples. They are confronted to an NMR 1D-imaging melting temperature study (section 4.5) and to Environmental Scanning Electronic Microscopy (ESEM) observations of the leached samples (section 4.7).

2. Materials

Three synthetic bituminized materials varying by their embedded salts were studied. Sample preparation procedures (Figure 1) were optimized to recover a final mass percentage of salts of about 40 % in all materials. They all have been produced with the same bitumen composition (Azalt 70/100) and with the same operating conditions. Pure bitumen was inserted at a temperature of 140 °C at the beginning of a co-rotating twin screw extruder (Werner ZSK25WLE: L = 1000 mm, L/D = 40, C_l = 21.1 mm with L the length, D the screw diameter and C_l the centreline distance) operating at a screw speed of 70 rpm with a flow rate of 0.57 $kg.h^{-1}$. Sludge, which contained water with dissolved $NaNO_3$ and/or insoluble $BaSO_4$ grains, was inserted 5 cm further at room temperature. Toluene and surfactants were added at the same inlet to make the sludge-bitumen mixture more fluid. Four vapour outlets were used along the screw to enable water evaporation (remaining quantity < 1 % in the final products). Consequently, crystallisation of soluble salts occurred during the extrusion process. All the produced materials were thus composed of salt grains embedded in bitumen. Table 1 gathers the main parameters related to the chemical composition of the different samples. For the sake of clarity, S-type stands for samples that only contain soluble salts, I-type stands for samples that only contain insoluble salts and B-type stands for samples that contain both soluble and insoluble salts.

3. Methods

3.1. Leaching experiments

Leaching experiments were performed in 10 mm diameter NMR tubes in order to follow the progression of the wetting front as a function of time by 1D-imaging techniques. To prepare a sample, a handmade cylinder of material was slid down to the bottom of a NMR tube. The tube was placed in an incubator for about 45 min at 50 °C, a temperature which was found to enable matrix warping without causing salt sedimentation. This procedure permitted to recover a cylindrical

sample of about 15 mm of height that took on the tube walls without enclosing any air bubble. Finally, two millilitres of pure water were added on top of the sample to start the unidirectional leaching process. The floating water was not renewed but was temporarily withdrawn from the sample surface to perform the NMR analyses.

3.2. Water uptake measurements by NMR

Water uptake measurements were carried out at 20 °C with a Bruker Minispec Analyzer operating at 45 MHz for the ^{1}H resonance. Masses of infiltrated water were obtained from a pre-established calibration curve that relates the intensity of ^{1}H-NMR signal to water quantity. The T_2 of the ^{1}H-bitumen was always found to be more than 20 times smaller than the T_2 of the infiltrated solution. Therefore, the intensity of the water signal was extracted from the overall NMR signal by analyzing CPMG data. They were acquired with an inter-pulse delay of 40 µs.

3.3. Water uptake measurements by 1D-imaging

All 1D-imaging experiments were performed at 20 °C on a 200 MHz Bruker Avance spectrometer equipped with a ^{1}H magnetic field gradient probe (diff-30). Moisture depth-profiles were obtained with the spin echo imaging scheme depicted in Figure 2-A. The strength of the magnetic gradients was set at 3.6 G/cm, which led to a frequency gradient of 15.3 kHz/cm in the 1D-profiles, and the delay τ was set at 0.75 ms to avoid any contribution of the ^{1}H bitumen ($T_2^{bitumen} \sim 200$ µs). In our samples, the smallest water T_2 values measured with a Hahn spin echo based sequence were about 7 ms. Therefore, more than 80 % of the water signal was always retained in the 1D-profiles. Such proportions were found to be large enough to interpret our results unambiguously.

3.4. Melting temperature measurements by 1D-imaging

For these experiments, the spectrometer was equipped with a Bruker BCU-X cooling unit. The real temperature in the sample was estimated from a pre-established calibration curve. Although no specific shielding of the sample was used to attenuate the thermal gradient along the sample height, the temperature control was found to be accurate enough to unambiguously characterise different ranges of water melting temperatures.

The NMR tube containing the sample was placed into the spectrometer at room temperature. Then, the temperature was decreased progressively down to 224 K and 1D-imaging experiments were thereafter regularly carried out under slow warming. Experiments were stopped when the entire water signal was recovered (at 270 K). With the help of preliminary tests, the temperature was increased by steps of about 1.5 K when the infiltrated solution was melting and by steps of about 7 K otherwise. The waiting time between two steps was determined by the time needed to obtain a fully stabilized NMR signal intensity (~ 15 min, typically). At each step, the radio-frequency (RF) coil was tuned and the RF pulses were re-calibrated before any acquisition. Then, the intensities of the obtained depth-profiles were corrected according to the temperature dependency of the RF coil sensitivity, as estimated from the length of the 180° pulse. The signal intensities were thereafter multiplied by the sample temperature at which they were acquired in order to account for Curie's law. As shown later, the so-corrected depth-profiles obtained between 224 K and 254 K were found to be the same. Even at low temperatures, T_2 values were therefore large enough to have negligible effects on the depth-profile intensities and shapes.

3.5. Self-diffusion and relaxation experiments with 1D-imaging detection

3.5.1. Description of the method

The approach used to measure the relaxation times and the self-diffusion coefficients of the infiltrated water along its depth concentration profile is schematically represented in Figure 2. It consists in performing classical ^{1}H relaxation or self-diffusion experiments with the previously

described 1D-imaging acquisition scheme (Figure 2-A). As a result, a series of depth-profiles weighted by the measured NMR parameter are obtained (Figure 2-B).

To analyse such a series of data, different processing strategies can be employed. For samples in which few populations present well-contrasted T_1, T_2 or D_S values (e.g. two different species), one can treat the whole 1D-profiles with multichannel methods such as CORE [17]. Doing so, the discrete values of the measured NMR parameter and their associated depth-profiles are directly obtained. However, such a method is no longer suited when the values of the studied NMR parameter are expected to evolve with sample depth. This is typically the case when, as in the present study, drying or infiltrating processes are investigated. We have therefore resorted to another approach which consists in dividing the depth-profiles in slices of about 200 µm (Figure 2-B) and processing the signal for each slice (Figure 2-C). This procedure allowed us to plot the evolution of the measured parameter as a function of depth, i.e. as a function of the local concentration of infiltrated water (Figure 2-D). Moreover, as illustrated in the example given in Figure 2, the use of two distinct populations in the fitting equations was sometimes needed to fully describe the NMR signal evolution. In such cases, the relative proportions recovered from the fitting in each slice were used to build-up the depth-profiles associated to each water population (Figure 2-E).

Using such an approach has several consequences that should be briefly highlighted. In contrast to methods that rely on selective excitation of sample slices, the spectral resolution is lost. A second drawback is that the signal processing procedures have to be implemented in computer programmes to automate them. However, this method also presents some advantages. Different populations can be differentiated as soon as they exhibit contrasts in the studied NMR parameter. If the spectral resolution is lost, different species may thus still be quantified. The experimental set up is flexible and very easy to prepare since it only requires modifying the acquisition scheme of an existing NMR pulse-sequence. Consequently, the overall acquisition time remains the same. Finally, it is

196 also noteworthy that the strength of the gradients used for the 1D-imaging acquisition is small
197 enough (about 3.6 G/cm in our experiments) to be implemented on any NMR spectrometer
198 equipped with a liquid coil, hence enabling, at least, spatially resolved characterisation of the
199 relaxation times.
200
201 *3.5.2. Experimental conditions and processing*
202
203 For all samples, the same approach as that illustrated for T_2 measurements in Figure 2 was used to
204 characterise the depth-dependency of the water:
205 - longitudinal relaxation time, T_1, measured with an inversion-recovery (IR) based sequence.
206 - self-diffusion coefficient, D_s, measured with a pulsed field gradient stimulated echo (PFG-STE)
207 based sequence [18]. It is noteworthy that, before running these experiments, we evaluated the
208 strength of the local gradients that may exist in our samples by measuring the transversal relaxation
209 time, T_2, of the water using CPMG sequences at different magnetic fields: at 1 T (^{1}H-45 MHz) and
210 at 4.6 T (^{1}H-200 MHz). Results showed that they were independent on the magnetic field, which
211 means that internal background gradients were very weak [19]. Therefore, we did not resort to a
212 pulse sequence that is specifically designed to reduce systematic errors induced by background
213 gradients [20]. We preferred to use the more compact STE sequence with a τ value as short as
214 possible in order to minimize the transverse relaxation effects.
215
216 The recycle delay was set at 5 T_1 in all experiments. T_1 measurements were conducted with 20
217 recovery times varying between 1 ms and 6 T_1. Depending on the sample type, the fitting equations
218 accounted for one or two discrete values of T_1. Besides, within a self-diffusion coefficient
219 measurement, 32 different gradient strengths, g, were used while keeping a constant diffusion
220 interval, Δ. The gradient strength was varied from 0 up to 1200 G/cm. The gradient length, δ, was
221 set at 1 ms and the recovery time after a gradient pulse was set at 2 ms. For all samples, the
222 dependency of the self-diffusion coefficients with the diffusion interval was then characterised by

varying Δ from 10 up to 1200 ms. Since our 1D-acquisition scheme remained always identical, the echo attenuation obtained with our NMR sequence within a slice was described, as for usual PFG-STE experiments, by the following relation:

$$I / I_0 = \sum_i p_i \exp\left(-k\, D_{Si}(d)\right) \quad \textbf{(1)}$$

with

$$k = \gamma^2 g^2 \delta^2 \left(\Delta - \delta/3\right) \quad \textbf{(2)}$$

I and I_0 are the signal intensities with and without magnetic gradients, respectively. γ is the gyromagnetic ratio, g the amplitude of the gradient pulse, δ the gradient pulse duration and Δ the time between the leading edges of the gradient pulses. $D_{Si}(d)$ is the self-diffusion coefficient of the i^{th} component within the slice at sample depth d, p_i the fractional proton number of the i^{th} component, and $\Sigma p_i = 1$. In the present study, i is equal to one or two.

All data processing were conducted with home-made programmes running on Matlab software. All fits were performed by nonlinear least-square methods. Noise simulations with a Monte-Carlo algorithm were used for error estimations of fitting parameters with 200 iterations.

3.6. ESEM

ESEM analyses were performed after NMR characterisations of the leached matrices in order to compare both data sets. Samples were prepared as follows. NMR tubes were broken after vertical notching with a glass-cutting knife in order to separate the glass from the bitumen. Samples were thereafter stored at -4 °C for 10 min to avoid sticking problems when removing the remaining glass pieces. The recovered materials were stored again at -4 °C during 5 min to harden the bitumen and were finally fractured along the cylindrical direction. Observations of their inner structure were thus conducted in the perpendicular direction to the leaching axis.

Material structures were characterised before and at the end of the leaching experiments by Environmental Scanning Electron Microscopy (FEI Quanta 200 ESEM FEG) coupled with a Bruker SDD 5010 energy dispersive spectrometer. The observation conditions were a 15 kV acceleration voltage and a 15 % relative water humidity in the chamber, the sample temperature being held at 3°C with a Peltier stage. These experimental conditions were optimised to avoid any modification of the sample microstructure during the analysis. Unleached samples were studied with a backscattered electron detector to enhance the phase contrast between bitumen and salts. The leached matrices were systematically observed as-prepared and after removal of the salts in an ultrasonic bath (water temperature close to 0 °C). Those presented in this paper were recorded with a large-field detector after the removal of salts to highlight structural relief and hence better characterise the topology of the altered microstructures.

4. Results and discussion

4.1. Characterisation of the unleached samples

Before running the leaching experiments, the three types of samples were characterised using Environmental Scanning Electron Microscopy coupled with energy dispersive spectrometry and a granulometry technique. For this latter analysis, a toluene extraction and an ultrasonic treatment of the embedded salts were applied in order to characterise the size distribution of the grains. Mean grain diameters in volume were obtained by performing laser particle analyses. Results are gathered in Table 1 for the three types of samples. Besides, in order to check sample homogeneity out, no less than five distinct zones were systematically observed by ESEM for each sample. The spatial dispersion of the grain salts appeared to be homogeneous within all materials. Examples of ESEM images and particle size distributions are reported in Figure 3 and Figure 4 for the S- and I-type samples, respectively.

In the S-type sample, $NaNO_3$ grains were single-crystals (Figure 3). In good agreement with the distribution centred at 31.5 µm obtained using laser particle analysis, most of them presented sizes of several tenths of micrometres. In the I-type material, the mean grain size and the distance between nearby grains were much smaller since they both appeared to be about few micrometres (Figure 4). Moreover, high magnification images of this sample indicate that $BaSO_4$ particles were in fact formed by an agglomeration of nanometric mono-crystals (see insert in Figure 4). The same type of aggregates was also observed in the B-type sample. Therefore, these results suggest that the $BaSO_4$ size distributions obtained by laser granulometry were mainly representative of these clusters. The B-type sample which was constituted by both kinds of salt showed a bimodal distribution centred at 13.5 and 2.9 µm which were attributed to $NaNO_3$ mono-crystals and $BaSO_4$ agglomerates, respectively. Mean particle sizes were different in the B-type materials because sample preparation procedures were optimised to recover a same mass percentage, and not grain size, of salts in all matrices.

4.2. Water uptake – Overall values

Figure 5 presents the kinetics of water uptake for the different types of samples as extracted from ^{1}H-NMR CPMG measurements. Results are average values obtained on 3 replicates for each type of material. These data confirm the surprising effect previously reported on samples of identical compositions [21]: richer samples in insoluble salts ($BaSO_4$) uptake more water. Indeed, after 190 days, the amount of water within the I-type material was about three times larger than in the S-type which exclusively enclosed soluble salts ($NaNO_3$). Accordingly, the B-type matrix, which was constituted by a mixture of both types of salt, presented an intermediate behaviour. Since all samples initially contained approximately the same volume of material (~ 0.9 cm^3), the overall water concentrations can be directly compared: after 190 days, they were in-between 15 and 50 $mg.cm^{-3}$ depending on the sample type.

4.3. Water uptake – 1D-profiles

Figure 6 presents the moisture depth-profiles measured by NMR 1D-imaging as a function of the leaching time for a S-, I- and B-type sample. Intensities, expressed in arbitrary units, are proportional to the absolute amount of water along sample depth, and the sample surface is indicated by the zero value on the abscissa. For S-type, all the water remained located within the first two millimetres of depth after 8 months of leaching. The 1D-profiles increased in intensity with the water uptake, whereas the penetration depth evolved very slowly and showed a well-defined wetting front. In the millimetres beneath the surface of the I-type sample, the increasing amount of water was comparable to that observed for the S-type matrix. However, the moisture progression within the sample was much faster since it reached the bottom of the NMR tube in less than 8 months. The local minimum observed at 5 mm in the 8-month depth-profile can probably be ascribed to a local zone that remained unleached. For the matrix containing both $NaNO_3$ and $BaSO_4$

314 salts, the depth-profiles were first similar to those obtained for the S-type sample (47 days) and
315 became more alike those characterised for the I-type sample at long leaching time.
316
317 These results clearly prove that $BaSO_4$ salts facilitate the water transport through the hydrophobic
318 materials, thereby explaining why samples richer in $BaSO_4$ uptake more water. The microscopic
319 mechanism for this effect is not currently well understood because several parameters should be
320 considered altogether. Indeed, the granulometry of the salts is important since for a given salt
321 volume fraction, smaller grains will be closer to each other and hence facilitate the water
322 progression, but in the meantime, the physical-chemistry of water in interaction with a highly and/or
323 a very poorly soluble salt is different and should also be considered. Besides, the present results
324 neither provide any knowledge on the water-salt interactions nor on the structures in which the
325 aqueous solution is located. Therefore, we then undertook to characterise the relaxation times and
326 the self-diffusion coefficients of the water along the depth-concentration profiles.
327
328 4.4. Longitudinal relaxation times, T_1
329
330 Figure 7 presents the T_1 values measured along the depth-profiles for the S- and I-type samples after
331 6 months of leaching. Experiments realised at other leaching times always showed a similar
332 evolution of the T_1 values with the water concentration. These results can therefore be considered as
333 representative of all our observations. For both samples, a unique T_1 population was characterised.
334 The discrete values evolved in the same way as a function of sample depth: they remained constant
335 in the first millimetres before decreasing in a very large extent when approaching the unleached
336 zone. Such decreases in T_1 indicate that the molecular motions of the water molecules were greatly
337 slowed down in the vicinity of the wetting front. We may therefore attribute these effects to an
338 increasing hindrance of molecular motions induced by a decreasing scale of porosity. For the S-type
339 sample, the plateau value was about 2.3 s. This is a feature of bulk $NaNO_3$ unsaturated water (Table
340 2). As for the I-type sample, the plateau value was about 1.5 s. Since $BaSO_4$ salts are poorly

soluble, we may have rather expected a value closer to that of neat water, i.e. T_1 ~ 3 s (Table 2). Several hypotheses can explain such a difference but, as it will be now shown, the most interesting point is that the aqueous solutions within the S- and I-type samples presented well-distinct T_1 values.

The same types of experiments were conducted on the B-type sample after 8 months of leaching. As presented in Figure 8, two T_1 components, and hence two types of water were distinguished. The largest component, T_{1A} (Figure 8-A), was also the most abundant since the T_{1A} population represented the quasi-totality of the overall 1D-profile (Figure 8-B). The concentration and the relaxation times of the T_{1A} population evolved likewise with depth: a sharp diminution in the millimetre beneath the sample surface followed by a more gentle decrease. Interestingly, the results obtained within these two ranges of depth were similar to those determined for the S- and I-type samples (Figure 7), respectively: a peak in the 1D-profile associated with T_{1A} values characteristic of bulk $NaNO_3$ salted water close to the surface, and a convex arc-shape profile associated with T_{1A} values between 1 and 1.5 s deeper in the material. The second component, T_{1B}, was of about 500 ms (Figure 8-A) and in an equivalent amount of water all over the leached zone (Figure 8-B). Since no such T_1 values were observed in the S- and I-type samples, this water population may reflect the occurrence of a coupled effect between $BaSO_4$ and $NaNO_3$ salts.

These results illustrate the benefits that can be drawn from the combination of NMR measurements with 1D-imaging experiments. Local concentration and relaxation times showed excellent correlations, and thereby provided straightforward interpretations for the T_1 values. Results also show that the behaviour of the T_{1A} population in the B-type material appears to be a convolution of those characterised for the single-salt matrices. The interpretation for the T_{1B} values remains less obvious. In fact, one may even wonder whether this population really exists or is the result of an inappropriate data processing. Accordingly, an investigation of the water melting temperature by

1D-imaging was thereafter initiated in order to validate the present results by uncoupling salinity and structural effects.

4.5. Melting temperatures in the B-type sample

For the 8-month leached B-type sample, the depth-dependency of the water melting temperature was characterised by collecting depth-profiles from 224 K up to 270 K. Figure 9 presents four of the 1D-profiles within that temperature range. Three main types of water were characterised. First, at 224 K, the lowest temperature we could reach, a fraction of the water remained liquid and unmodified until the sample was warmed up to 255 K. Such an extent of surfusion can only be explained by a small-scale porosity effect [22]. Besides, this water population was remarkably similar both in terms of depth-profile's quantity and shape to the characterised T_{1B} population (Figure 8). It thereby provides an original validation of the T_1 results as well as a straightforward explanation for the previously described small T_{1B} values (~ 500 ms): the small-scale porosity hinders the motions of water molecules. Second, an arc-shape depth-profile presented a melting temperature of about 257 K. In good agreement with the 255.5 K found in the literature [23], this melting temperature is a feature of bulk $NaNO_3$ saturated water. The third population concerns the water peak beneath the sample surface that presented a distribution of melting temperatures from 257 up to 270 K. This observation is in excellent agreement with our T_{1A} results since it unambiguously proves that all the water beneath the surface was not saturated with $NaNO_3$. Moreover, these results also provide an important information on the leaching behaviour of BWP:

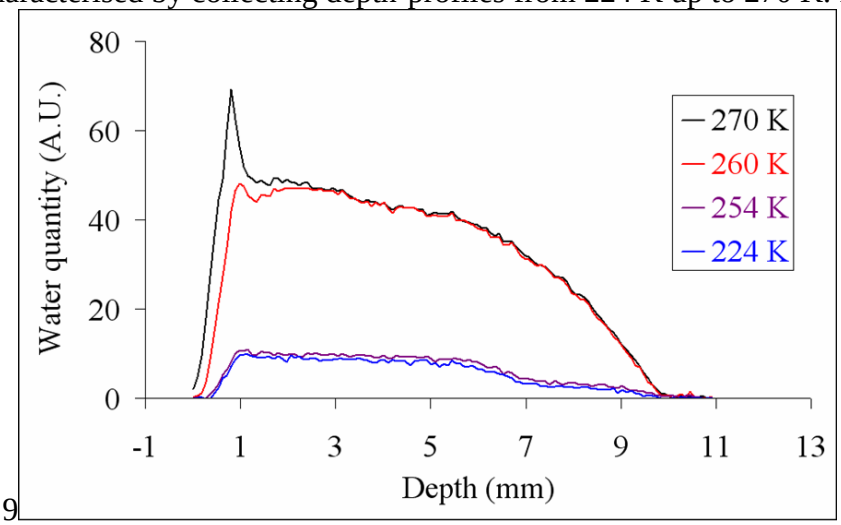

9

386 in contrast to what was previously supposed [15], the water progression in depth is not necessarily
387 limited by the dissolution of $NaNO_3$ salts.
388
389 In conclusion, the three aqueous populations characterised by different ranges of T_1 in the B-type
390 sample (Figure 8) could be discriminated by their melting temperatures, and confrontation of both
391 sets of results provided coherent explanations for the measured T_1 values as well as new elements to
392 better understand the leaching of BWP by water.
393
394 4.6. Self-diffusion coefficients
395
396 In the following paragraphs, data obtained for the S-type matrix after 6 months of leaching will be
397 used as an example to illustrate how spatially resolved self-diffusion experiments provided useful
398 information on our systems. The self-diffusion coefficients determined along the moisture
399 concentration profile for a short diffusion interval, Δ = 10 ms, are presented in Figure 10. Two
400 different diffusing water populations were observed. The first one presented self-diffusion
401 coefficients, D_{SA}, ranging from 0.9 to 1.8 $\times$ 10^{-9} m^2/s. In accordance with previously described
402 results, these values are characteristic of bulk $NaNO_3$ salted water (Table 2), while the progressive
403 decrease of D_{SA} with depth can be simply explained by a converse increase in water salinity. The
404 second population presented self-diffusion coefficients, D_{SB}, so small that a microstructural
405 hindrance of the molecular motions has to be considered. In other words, these values are more
406 related to the microstructure of the aqueous network than to the solution properties. To better
407 characterise this structural effect, other measurements were carried out with increasing diffusion
408 interval, Δ, in order to let water molecules probe larger distances within the sample. For each water
409 population, the root mean square displacement (RMSD) was then calculated using the following
410 relation:
411 $$RMSD(\Delta, d) = \sqrt{2\,\Delta\,D_S(\Delta, d)} \quad \textbf{(3)}$$

412 with $D_S(\Delta, d)$ determined from Eq. (1-2). The so-determined RMSD are presented as a function of
413 both Δ and sample depth in Figure 11.
414
415 For population A (top part of Figure 11), the RMSD never stopped increasing and was of about 40
416 µm at Δ_{max} = 1.2 s. Therefore, these water molecules were evolving in an open network over several
417 tens of micrometres. However, the diffusion coefficients did not remain perfectly constant with Δ,
418 and hence, the RMSD did not perfectly obey a root-law [see Eq. (3)]. For instance, at 1.65 mm of
419 depth, D_{SA} decreased from 1.6×10^{-9} to 1.1×10^{-9} m²/s when Δ was increased from 10 ms to 1.2 s.
420 This deviation from a Fickian behaviour can be explained by considering that water molecules
421 encountered structural heterogeneities in the range of the length-scales probed, i.e. from a RMSD of
422 about 2 µm to about 40 µm. Nevertheless, whatever the diffusion interval, the diffusion coefficients
423 D_{SA} were always about or superior to 1.0×10^{-9} m²/s, which remains close to the solution bulk
424 properties (Table 2). Therefore, these values proved that few obstacles were encountered during the
425 diffusing process, i.e. the tortuosity was low at the micrometre scale.
426
427 For population B however (bottom part of Figure 11), the RMSD did not increase beyond 9 ± 1 µm
428 whatever the sample depth. This behaviour is typical of the so-called total restricted diffusion
429 phenomenon [24, 25]. The water molecules cannot probe larger distances because they are located
430 in a closed geometry during the time-scale of the experiments. By assuming spherical pores, one
431 may calculate a mean pore diameter, Φ_{mean}, when the RMSD plateau value is reached, with the
432 following equation [25]:
433
$$\Phi_{mean}^2 = 20\ D_S(\Delta, d)\ \Delta \qquad \textbf{(4)}$$

434 This leads to a mean closed pore diameter of about 30 µm whatever the sample depth.
435
436 The same experimental and analysing procedures were used to investigate the I- and B-type samples
437 after 6 months of leaching. For both types of material, the coexistence of closed pores with an open

438 network was also characterised at the micrometre scale. For the I-type sample, the water population
439 located in an open network presented self-diffusion coefficients that were independent of the
440 sample depth and of about 0.7×10^{-9} m²/s. For this material, we may consider that the water was
441 pure since the solubility of $BaSO_4$ is negligible. However, 0.7×10^{-9} m²/s is about three times
442 smaller than the 2.3×10^{-9} m²/s of pure water (Table 2). This smaller effective self-diffusion
443 coefficient can thus be attributed to a highly tortuous structure (twisted diffusion pathways). For the
444 second population, the RMSD remained the same whatever the diffusion interval we used, the
445 shortest being 10 ms. This means that the water molecules had enough time within these 10 ms to
446 entirely explore the vicinities of the closed pores. Therefore, the mean pore size was too small to be
447 properly extracted [26] even if it provides evidence of an upper limit around one or few microns.
448 For the sample containing both $NaNO_3$ and $BaSO_4$, the water population located in an open network
449 presented self-diffusion coefficients that decreased from 1.6 to about 0.5×10^{-9} m²/s in the first two
450 millimetres and remained constant beyond. The micrometric tortuosity of the open network was
451 thus low close to the surface but high in deeper areas. The second water population was evolving in
452 closed porosities. Their mean diameter was estimated to be 16 µm using Eq. (4).
453
454 Table 3 summarizes the results we were able to extract from the self-diffusion experiments. Beyond
455 corroborating previous findings on the water salinity, the present results provide fruitful information
456 on the leached microstructures. The mean diameter values we obtained are comparable to the sizes
457 of the grain salts (or clusters) initially enclosed in the three matrices (Table 1). For the S-, I- and B-
458 type sample, mean sizes of 31.5, 5 and 13.5 µm were recovered by laser particle analyses and mean
459 pore diameters of 30 µm, less or about one or few microns and 16 µm were determined from self-
460 diffusion experiments, respectively. Even if the water ingress had necessarily modified the inner
461 structure of the samples, the equivalence seems rather good. Tortuosity results can also be related to
462 the properties of the embedded salts. Indeed, the dissolution of the $NaNO_3$ grains leads to
463 micrometric empty spaces, and hence entails the formation of a slightly tortuous microstructure.

This is consistent with what we observed in the S-type material and in the upper part of the B-type material since the dissolution of $NaNO_3$ salts was more advanced in that sample zone. Similarly, the highly tortuous structure observed in the I-type sample and in the deeper part of the B-type material can be explained by considering that, given their insoluble character, aqueous porosities were filled with nanometric $BaSO_4$ crystals. All the present results can thus be interpreted by taking into account the physical-chemistry of each kind of salt. Moreover, it is noteworthy that comparison of all these structural findings with T_1 results indicates that the porous microstructures and the water relaxation properties were closely related: the more tortuous the structure, the smaller the T_1 values (Figure 7 and Figure 8). We may therefore state that the properties of the different kinds of salt entail the formation of different types of water-filled structures, which in turns result in water populations that present different ranges of T_1 values. Even if all these conclusions seem reasonable, ESEM analyses were launched to confront our interpretation of the self-diffusion results to a direct observation of the leached microstructures.

4.7. ESEM

Samples were studied by environmental scanning electron microscopy after 11 months of leaching. Systematic investigations were performed on the water/sample interface (upper part of the sample), on the leached zone (middle part) and on the remaining unleached zone when it existed (lower part of the sample). Figure 12 shows the general features of the microstructures observed at a same magnification.

ESEM analyses performed on the S-type matrix were in good agreement with the NMR 1D-imaging results (Figure 6) since the leached zone ended at about 2 mm. Morphology comparison between the unleached (Figure 3) and the 11-month leached material (Figure 12-S) illustrates the strong impact of the water ingress on the sample microstructure. In good accordance with previously reported data [14], the leached structure consisted in spherical pores having diameter ranging from

few micrometres up to several tens of micrometres. As illustrated in Figure 13-S, we also observed that part of these pores, at least, seemed to be interconnected (note that the salt grains observed in this figure result from a $NaNO_3$ re-crystallization that followed the imperfect washing of the sample surface by pure water).

The leached structure of the I-type sample was very different. Within that material, the leaching process yielded to the formation of a homogenous network that had progressed from the water/sample interface down to the bottom of the bitumen cylinder. This network consisted in micrometric channels that appeared to be interconnected in three dimensions (Figure 12-I). Observations made before removal of salts demonstrated that these channels were entirely filled with $BaSO_4$ particles (data not shown). Moreover, an adjacent type of structure, which consisted in a dispersion of small pores containing some $BaSO_4$ agglomerates, was observed at a higher magnification (Figure 13-I). The great majority of these pores presented diameters in the range of few hundreds of nanometres up to few micrometres.

The long-term water contact with the B-type matrix yielded to the formation of a complex microstructure. Close to the water/sample interface (upper part of Figure 12-B_1), we observed a morphology very similar to the one observed in the S-type bitumen. Spherical pores as well as some interconnections between them could indeed be observed in that sample zone. Differences in the apparent pore sizes in the S- and B-type leached samples can be related to the differences in the sizes of $NaNO_3$ crystals in unleached materials (Table 1). Nevertheless, the bottom part of Figure 12-B_1 shows that a second type of structure also co-existed. This sponge-like morphology progressively evolved with depth towards a more network-like structure (Figure 12-B_2) very similar to the one observed in the I-type sample, and which also enclosed $BaSO_4$ particles (data not shown). The smaller density of channels in the B-type matrix can be easily explained by its smaller content in $BaSO_4$ (Table 1). In agreement with our self-diffusion results, no small pores such as those observed in Figure 13-I could be observed in the B-type sample.

Evidences of an open network coexisting with isolated pores were found in all matrices using ESEM. The so-observed structures are all in line with the open network tortuosities and the mean diameters of closed pores previously determined (Table 3). They also confirm that $NaNO_3$ and $BaSO_4$ effects were of different extents as a function of the sample depth in the B-type material. Therefore, all the features obtained by ESEM provide an elegant validation of the self-diffusion results and interpretations.

5. Conclusion

Original NMR designed experiments have been set up to characterise the relaxation times and the self-diffusion coefficients along the depth-concentration profile of a solution infiltrated in a soft porous medium. This approach was found to be particularly efficient to study three synthetic bituminized waste products over several months of leaching. It was shown that the water uptake and the water concentration profile depend on the salt composition. Indeed, both $NaNO_3$ (soluble salt) and $BaSO_4$ (insoluble salt) were found to have a specific influence on the moisture transport and on the associated altered structure. When a mixture of both kinds of salt was embedded in bitumen, our results showed that these specific effects are essentially superimposed and are well disclosed with our NMR approach.

On the one hand, our results provide new elements to better understand how water progresses into bituminized waste products and hence, how embedded elements can leach out of these materials. In particular, for matrices made of both $NaNO_3$ and $BaSO_4$, the progression of the wetting front was believed to be limited by the dissolution of $NaNO_3$ and the insoluble salts were thought to have a negligible influence. Our results invalidate both hypotheses. Therefore, an updated version of the phenomena that take place during the leaching of these materials needs to be described. On the other hand, this study demonstrates that performing NMR measurements with 1D-imaging

detection can become a valuable tool to study infiltrating and drying processes in porous systems, and more generally, to investigate phenomena that can progress with a cylindrical symmetry.

Acknowledgements

The authors are grateful to Agnes Barré and Marc Masson-Fauchier from the L2ED (CEA Marcoule) for the preparation and the characterisation of the unleached materials. Florence Bart, Aurélien Ledieu and Christophe Joussot-Dubien for very fruitful discussions. We also thank the SPrAM/PCI laboratory for the reception of Steven Le Feunteun during the construction of the Institut de Chimie Separative de Marcoule (ICSM), and finally the NMR laboratory of the Institut des Nanosciences et de Cryogénie (INAC, CEA Grenoble) for the availability of their spectrometer.

References

[1] Knorgen M, Arndt KF, Richter S, Kuckling D, Schneider H. Investigation of swelling and diffusion in polymers by H-1 NMR imaging: LCP networks and hydrogels. J Mol Struct 2000;554(1):69-79.

[2] Chen XM, Astary GW, Sepulveda H, Mareci TH, Sarntinoranont M. Quantitative assessment of macromolecular concentration during direct infusion into an agarose hydrogel phantom using contrast-enhanced MRI. Magn Reson Imaging 2008;26(10):1433-1441.

[3] Baille WE, Malveau C, Zhu XX, Marchessault RH. NMR Imaging of high-amylose starch tablets. 1. Swelling and water uptake. Biomacromolecules 2002;3(1):214-218.

[4] Erich SJF, Laven J, Pel L, Huinink HP, Kopinga K. NMR depth profiling of drying alkyd coatings with different catalysts. Prog Org Coat 2006;55(2):105-111.

[5] Erich SJF, Adan OCG, Pel L, Huinink HP, Kopinga K. NMR imaging of coatings on porous substrates. Chem Mat 2006;18(18):4500-4504.

[6] Kuntz M, Lavallee P. Experimental evidence and theoretical analysis of anomalous diffusion during water infiltration in porous building materials. J Phys D 2001;34(16):2547-2554.

[7] Jaffel H, Korb JP, Ndobo-Epoy JP, Morin V, Guicquero JP. Probing microstructure evolution during the hardening of gypsum by proton NMR relaxometry. J Phys Chem B 2006;110(14):7385-7391.

[8] Jaffel H, Korb JP, Ndobo-Epoy JP, Guicquero JP, Morin V. Multi-scale approach continuously relating the microstructure and the macroscopic mechanical properties of plaster pastes during their settings. J Phys Chem B 2006;110(37):18401-18407.

[9] Faure PF, Rodts S. Proton NMR relaxation as a probe for setting cement pastes. Magn Reson Imaging 2008;26(8):1183-1196.

[10] Collins JHP, Gladden LF, Hardy IJ, Mantle MD. Characterizing the evolution of porosity during controlled drug release. Appl Magn Reson 2007;32(1-2):185-204.

[11] McDonald PJ, Ciampi E, Keddie JL, Heidenreich M, Kimmich R. Magnetic-resonance determination of the spatial dependence of the droplet size distribution in the cream layer of oil-in-water emulsions: Evidence for the effects of depletion flocculation. Phys Rev E 1999;59(1):874-884.

[12] d'Avila MA, Powell RL, Phillips RJ, Shapley NC, Walton JH, Dungan SR. Magnetic resonance imaging (MRI): A technique to study flow an microstructure of concentrated emulsions. Braz J Chem Eng 2005;22(1):49-60.

[13] Hollingsworth KG, Johns ML. Spatially resolved emulsion droplet sizing using inverse Abel transforms. J Magn Reson 2005;176(1):71-78.

[14] Gwinner B, Sercombe J, Tiffreau C, Simondi-Teisseire B, Felines I, Adenot F. Modelling of bituminized radioactive waste leaching. Part II: Experimental validation. J Nucl Mater 2006;349(1-2):107-118.

[15] Sercombe J, Gwinner B, Tiffreau C, Simondi-Teisseire B, Adenot F. Modelling of bituminized radioactive waste leaching. Part I: Constitutive equations. J Nucl Mater 2006;349(1-2):96-106.

[16] Mokni N, Olivella S, Li XL, Smets S, Valcke E. Deformation induced by dissolution of salts in porous media. Phys Chem Earth 2008;33:436-443.

[17] Stilbs P, Paulsen K, Griffiths PC. Global least-squares analysis of large, correlated spectral data sets: Application to component-resolved FT-PGSE NMR spectroscopy. J Phys Chem 1996;100(20):8180-8189.

[18] Tanner JE. Use of stimulated echo in NMR-diffusion studies. J Chem Phys 1970;52(5):2523-2526.

[19] Gottwald A, Creamer LK, Hubbard PL, Callaghan PT. Diffusion, relaxation, and chemical exchange in casein gels: A nuclear magnetic resonance study. J Chem Phys 2005;122(3):034506.1-034506.10.

[20] Cotts RM, M. J. R. Hoch, T. Sun, J. T. Markert. Pulsed field gradients stimulated echo methods for improved NMR diffusion measurements in heterogeneous systems. J Magn Reson 1989;83:252-266.
[21] Le Feunteun S, Diat O, Guillermo A, Ledieu A, Poulesquen A. Leaching of bituminized waste products (BWP) by pure water: The contribution of NMR techniques for the investigation of the porous layer. In: MRS Symposium Proceedings: Scientific Basis for Nuclear Waste Management XXXIII. Vol. 1193 Saint Petersburg; 2009: p. 505-512.
[22] Petrov OV, Furo I. NMR cryoporometry: Principles, applications and potential. Prog Nucl Magn Reson Spectrosc 2009;54(2):97-122.
[23] Archer DG. Thermodynamic properties of the $NaNO_3$+H_2O system. J Phys Chem Ref Data 2000;29(5):1141-1156.
[24] Price WS. Pulsed-field gradient nuclear magnetic resonance as a tool for studying translational diffusion .1. Basic theory. Concepts Magn Reson 1997;9(5):299-336.
[25] Callaghan PT. Principles of Nuclear Magnetic Resonance Microscopy. Oxford: Oxford Science Publications, 1991.
[26] Guillermo A, Bardet M. In situ pulsed-field gradient NMR determination of the size of oil bodies in vegetable seeds. Analysis of the effect of the gradient pulse length. Anal Chem 2007;79(17):6718-6726.

Tables

Table 1: Chemical composition of the samples and mean particle diameter of the embedded salts determined by laser particle size analysis.

Sample-type	Incorporated salts, mass %	Salt, mass %	Salt, volume %	Mean salt diameter (µm)
S	100% $NaNO_3$	40.3	23.3	31.5 ± 13.2
I	100% $BaSO_4$	40.8	13.5	5 ± 3
B	33.3% $NaNO_3$ 66.6% $BaSO_4$	40.3	16.9	13.5 ± 7.5 2.9 ± 1.2

Table 2: Longitudinal relaxation time and self-diffusion coefficient of pure water and $NaNO_3$ saturated water at 20°C.

	T_1	D
Neat water	3 s	2.3×10^{-9} m²/s
Water saturated with $NaNO_3$	2.0 s	0.9×10^{-9} m²/s

Table 3: Mean diameter of the closed pores as well as information relative to the tortuosity of the open network and to the salinity of the solution as extracted from diffusion experiments.

	Mean diameter of closed pores	Tortuosity of the open network	Water salinity
S-type	~ 30 µm	Low	Unsaturated
I-type	< or ~ micron(s)	High	Necessarily ~ pure
B-type	~ 16 µm	Low in the 1st mm & High deeper	Unsaturated in the 1st mm

Figures

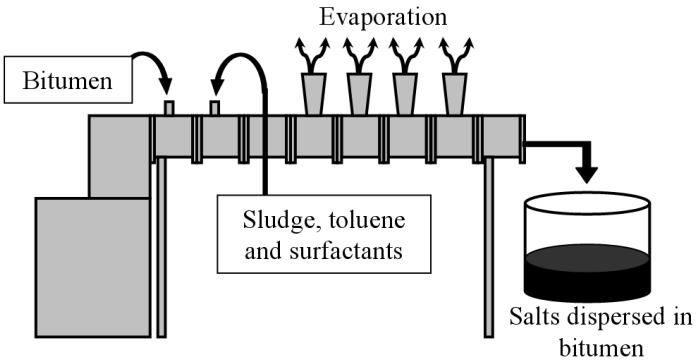

Figure 1: Schematic representation of the extrusion process used to prepare the samples. Final materials consist in soluble and/or insoluble salt grains dispersed in bitumen.

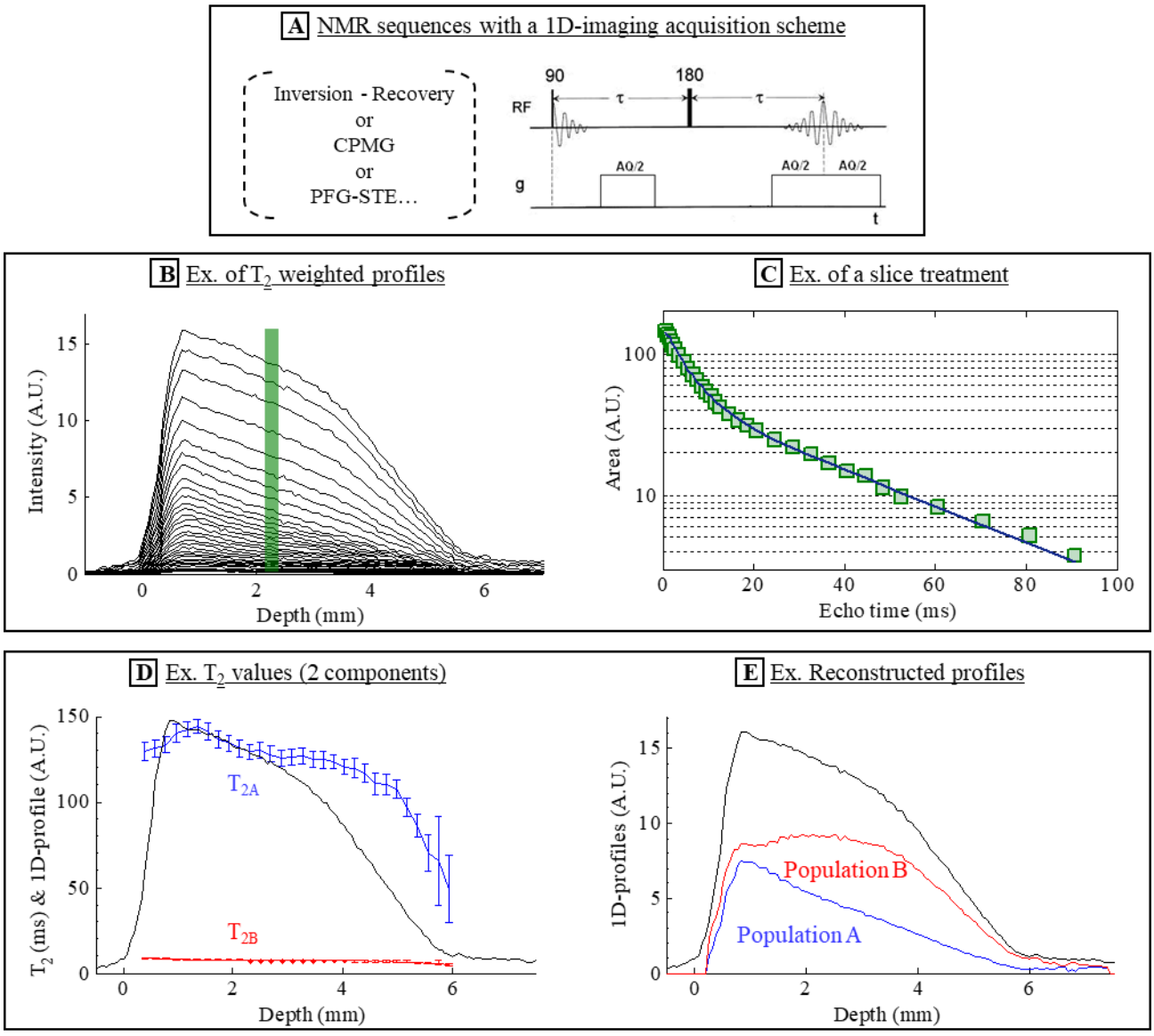

Figure 2: A) Schematic representation of the method used to measure the self-diffusion coefficients and the relaxation times as a function of sample depth. B-E) Example of T_2 measurements on a leached sample using a spin echo based sequence.

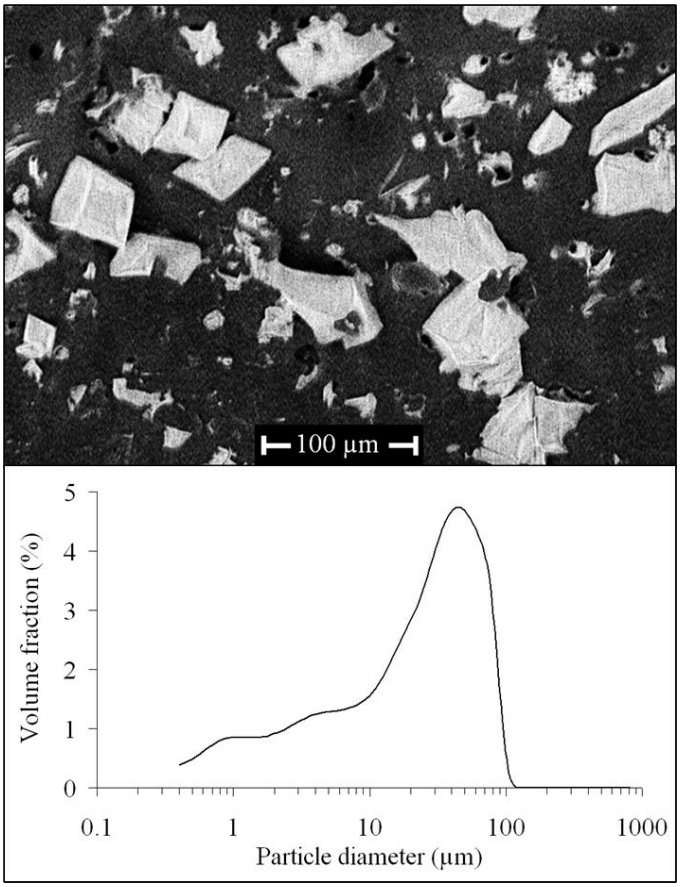

Figure 3: Examples of results obtained by ESEM and laser particle size analysis for the unleached S-type sample.

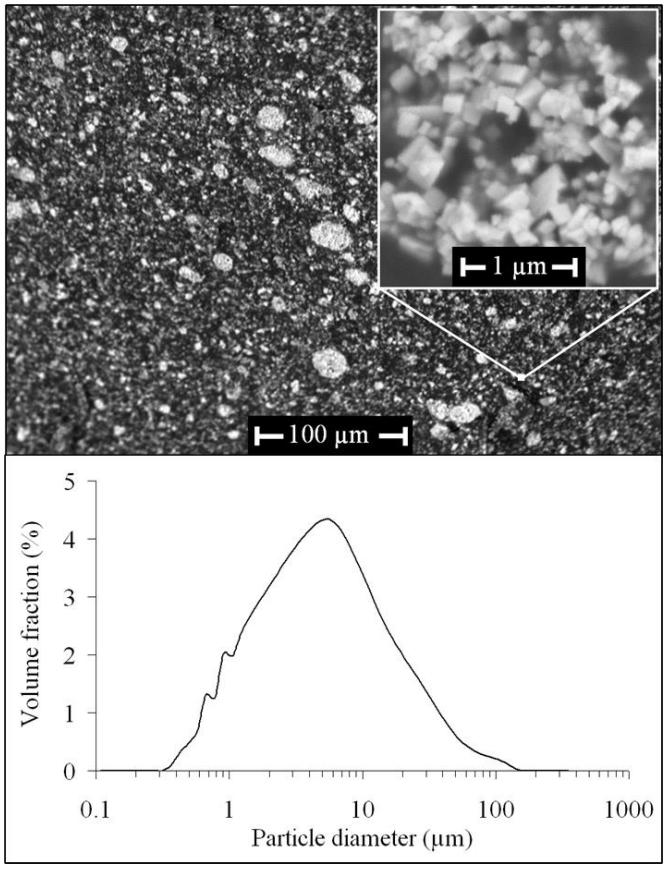

Figure 4: Examples of results obtained by ESEM and laser particle size analysis for the unleached I-type sample.

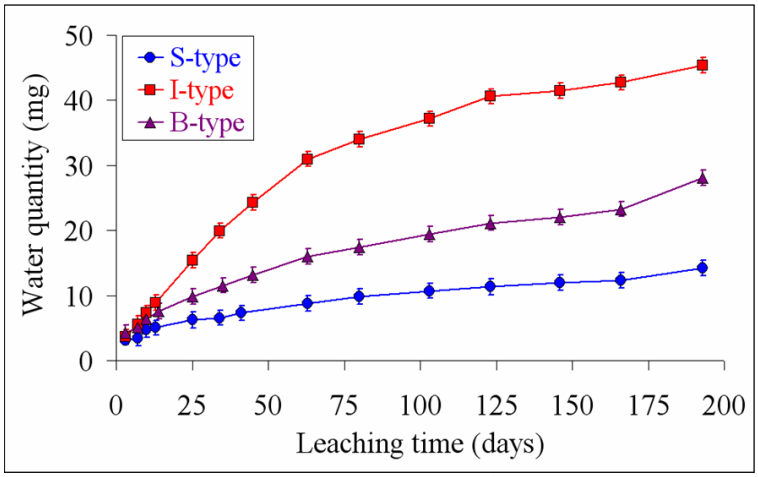

Figure 5: Average water uptake kinetics as extracted from ^{1}H-NMR CPMG data on three replicates of each sample type.

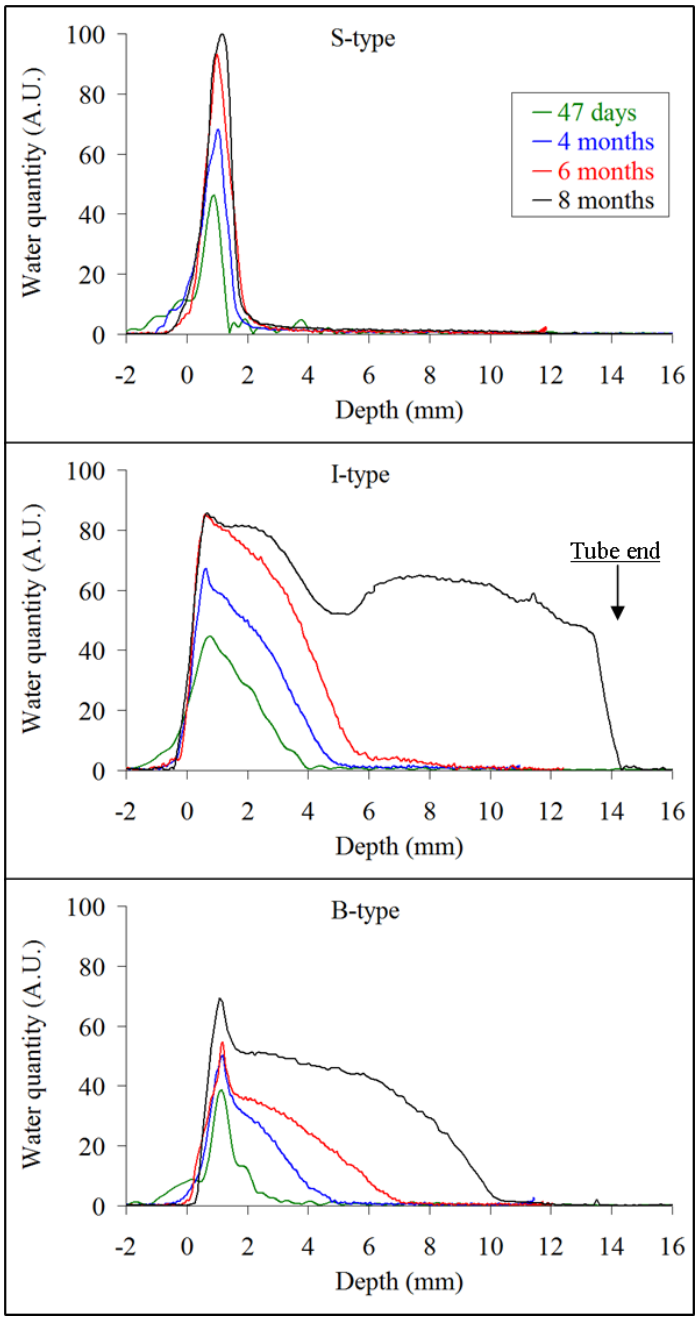

Figure 6: 1D-profiles after 47 days, 4, 6 and 8 months of leaching (from bottom to top) for each type of sample.

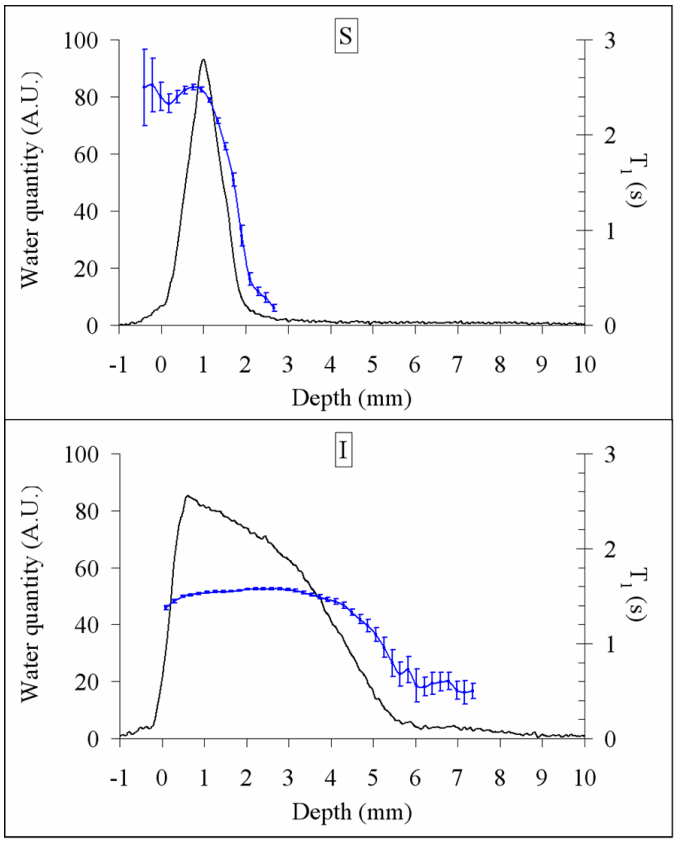

Figure 7: Longitudinal relaxation times, T_1, of the infiltrated water after 6 months of leaching as a function depth for the S- and I-type samples. Water concentration profiles are superimposed to the T_1 data.

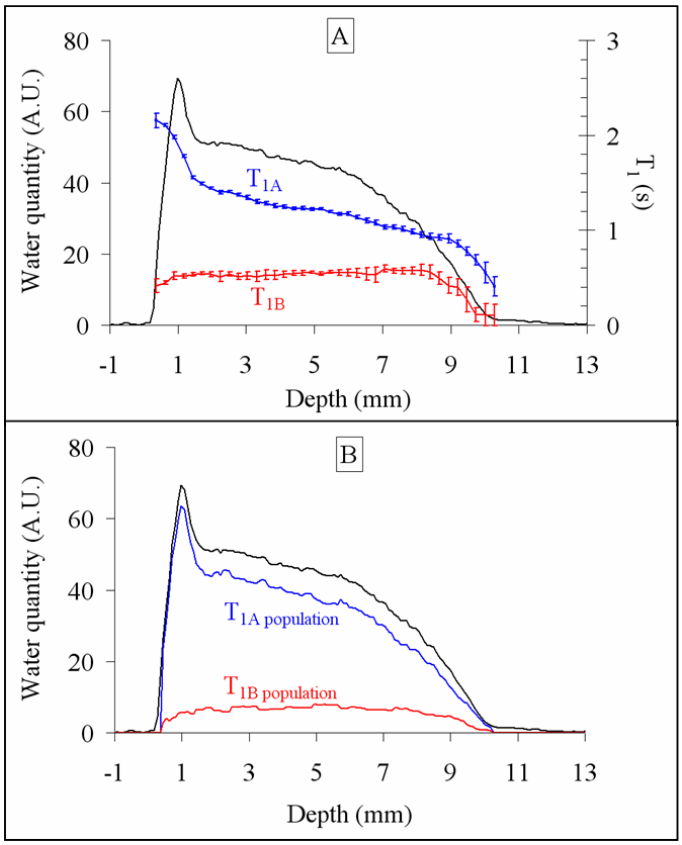

Figure 8: Longitudinal relaxation times, T_1, of the infiltrated water after 8 months of leaching as a function of depth for the B-type matrix: A) T_1 values and B) Reconstructed water concentration depth-profiles.

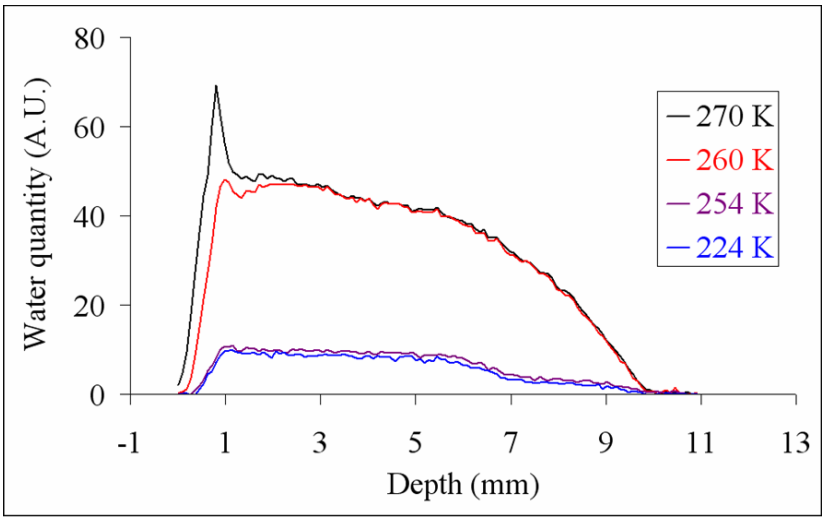

Figure 9: Evolution of the water depth-profiles for the 8-month leached B-type sample from 224 K up to 270 K (from bottom to top).

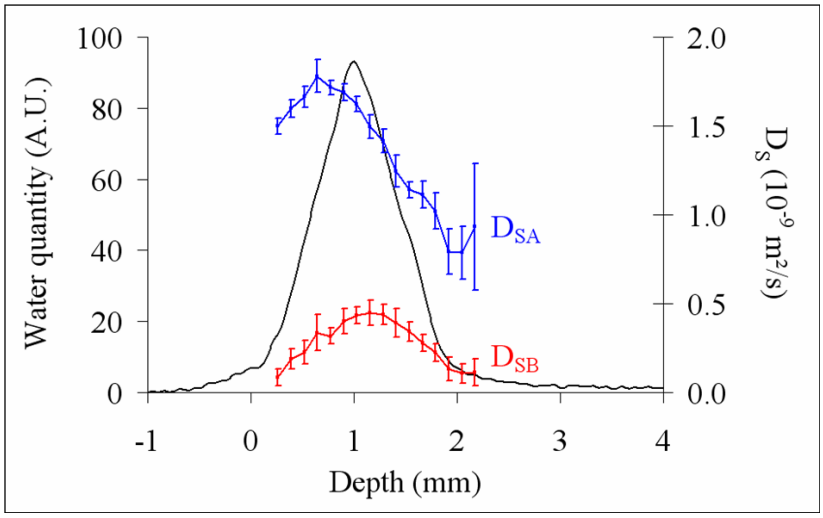

Figure 10: Self-diffusion coefficients of the infiltrated water measured with a diffusion interval of 10 ms as a function of depth for the S-type sample after 6 months of leaching.

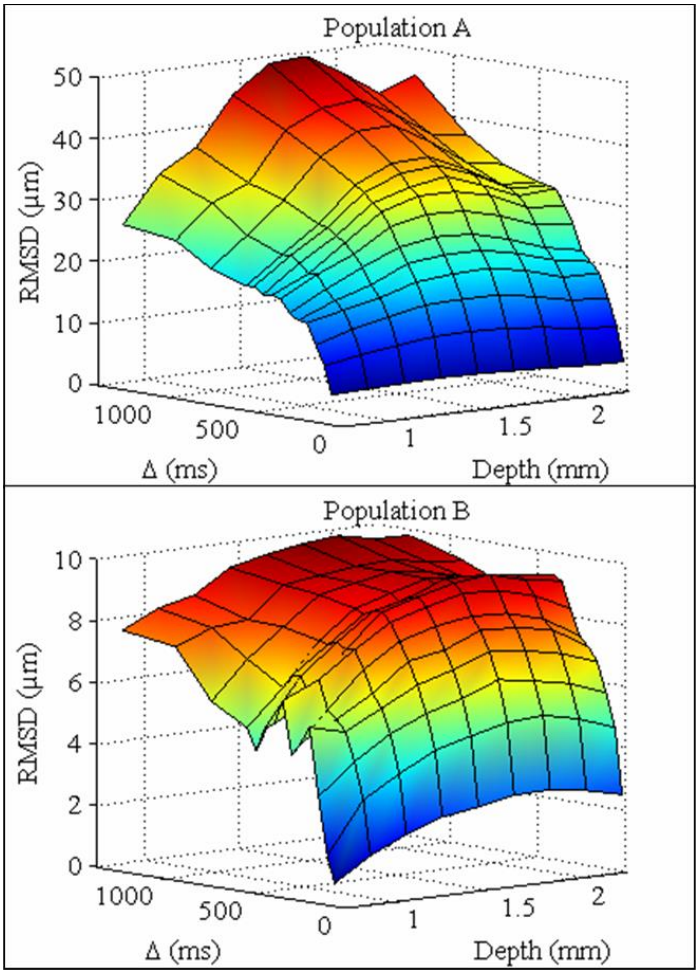

Figure 11: Evolution of the root mean square displacement (RMSD) of each water population as a function of both the diffusion interval, Δ, and the depth for the S-type sample after 6 months of leaching.

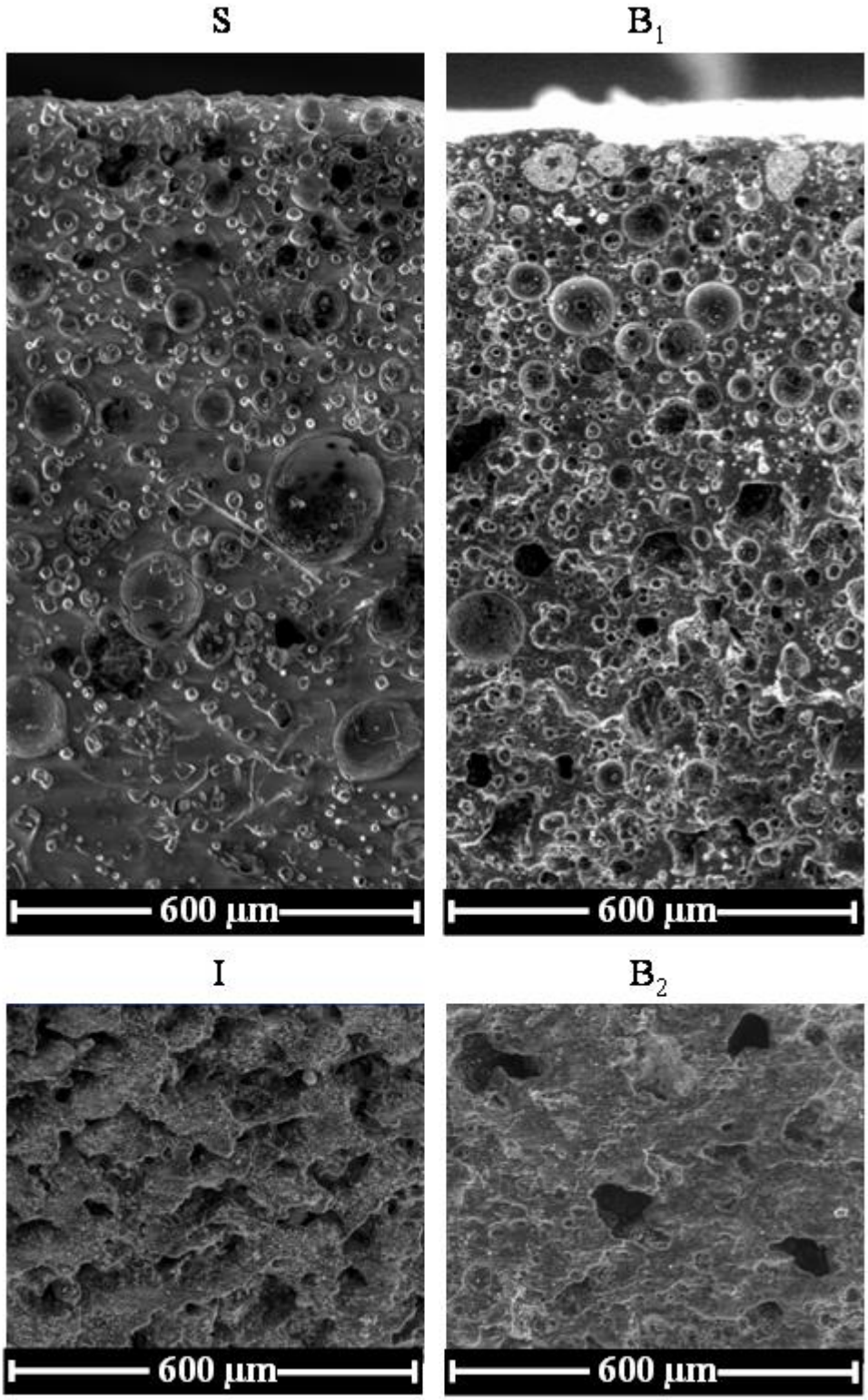

Figure 12: ESEM images at a same magnification of the samples after 11 months of leaching: S) S-type, I) I-type, B_1) B-type: top part, and B_2) B-type: at 4 mm of depth.

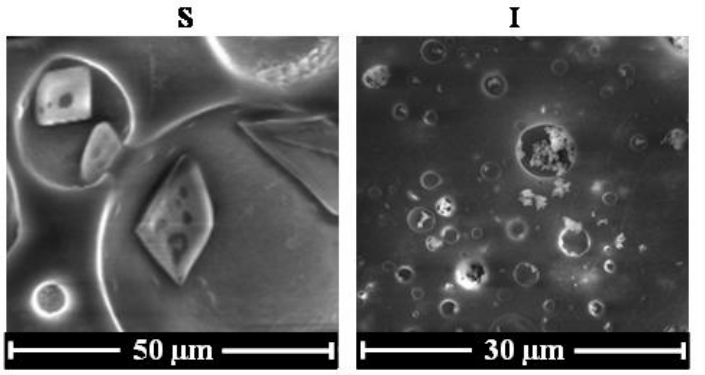

Figure 13: High magnification ESEM images of the samples after 11 months of leaching: S) S-type, and I) I-type.